Available online at www.sciencedirect.com
SCIENCE DIRECT®
International Journal of Heat and Mass Transfer 48 (2005) 4926–4941
International Journal of HEAT and MASS TRANSFER
www.elsevier.com/locate/ijhmt

# The structure of a double-diffusive interface in a laterally heated enclosure

J. Tanny [a], R. Dviri [b], A. Svizher [b], J. Cohen [b,*]

[a] Institute of Soil, Water and Environmental Sciences, Agricultural Research Organization, Volcani Center, P.O. Box 6, Bet Dagan 50250, Israel
[b] Faculty of Aerospace Engineering, Technion-Israel Institute of Technology, Haifa 32000, Israel

Received 26 April 2004; received in revised form 26 January 2005
Available online 15 August 2005

**Abstract**

Experiments are carried out to investigate the structure of a double diffusive interface separating two layers in a laterally heated enclosure. Due to the differential heating of the enclosure sidewalls, a circulating flow is induced in each layer such that the interface is simultaneously exposed to a velocity shear and double diffusive convection. The main goal of this work is to study the structure of the interface and some of its instability characteristics. The experiments are carried out in a box with inner length, width and height dimensions of $100 \times 100 \times 92$ mm. The velocity field at the vicinity of the interface is measured by a PIV system. Vertical concentration and temperature profiles are measured using a micro-scale conductivity/temperature instrument and the flow is visualized using the schlieren technique. Analysis of mean horizontal velocity profiles, obtained at different times during the experiment, illustrates the increasing tilt of the interface with time. Spectral analyses of velocity perturbations under unstable and stable conditions confirm the existence of the coherent vortices observed by the schlieren technique. The vortices above and below the interface are associated with different dominant frequencies due to the asymmetric character of the flow. Measurements show that the vortices are generated outside the region of the stabilizing concentration profile by a mechanism, which is essentially thermal and similar to Rayleigh–Bénard instability with weak shear.


*Keywords:* Stratified fluid; Stability; Velocity; Temperature; Concentration; Vortices

## 1. Introduction

The interface separating two layers of a solute-stratified fluid in a laterally heated enclosure is one of the fundamental double-diffusive systems. The interest in this system stemmed mainly from the fact that this interface is a basic element of more complicated double-diffusive multi-layered systems. For example, when a continuous stable solute gradient is subjected to a lateral temperature gradient (e.g., [1]) an array of convective layers separated by density interfaces is formed. Under certain conditions the layers undergo a sequence of merging events in each of which two adjacent layers merge into one thicker layer. Merging processes in such a system were studied by, e.g., Wirtz and Reddy [2],

* Corresponding author. Tel.: +972 4 8292312; fax: +972 4 8292030.
*E-mail address:* aerycyc@aerodyne.technion.ac.il (J. Cohen).

0017-9310/$ - see front matter © 2005 Elsevier Ltd. All rights reserved.
doi:10.1016/j.ijheatmasstransfer.2005.06.011

**Nomenclature**

$A_r = H/L$ aspect ratio of the enclosure [–]
$\Delta C$ concentration difference between the two layers [wt.%]
$f$ disturbance frequency [Hz]
$g$ acceleration due to gravity [mm/s$^2$]
$H$ height of the fluid [mm]
$L$ width of the enclosure [mm]
$Ra = g\alpha\Delta TL^3/\nu\kappa$ Rayleigh number [–]
$Ra_{bot} = \frac{g\alpha\Delta T_{bot}\delta_{bot}^3}{\nu\kappa}$ local Rayleigh number of the layer with positive density gradient below the interface [–]
$R_\rho = \beta\Delta C/\alpha\Delta T$ buoyancy ratio [–]
$R_{\rho l} = \frac{\beta\Delta C}{\alpha\Delta T_i}$ local buoyancy ratio [–]
$St = f\delta_m/U_m$ Strouhal number [–]
$t$ time [min]
$\Delta T$ lateral temperature difference [°C]
$\Delta T_{bot}$ vertical temperature difference across the layer of positive density gradient below the interface [°C]
$\Delta T_i$ vertical temperature difference across the interface [°C]
$u$ instantaneous horizontal velocity [mm/s]
$U$ mean horizontal velocity [mm/s]
$U_{max}$ maximum horizontal mean velocity (positive value) [mm/s]
$U_{min}$ minimum horizontal mean velocity (negative value) [mm/s]
$U_m$ the largest absolute value between $U_{max}$ and $U_{min}$ [mm/s]
$v$ instantaneous vertical velocity [mm/s]
$V$ mean vertical velocity [mm/s]
$X_d$ dimensional horizontal distance [mm]
$Y$ $Y_d - Y_{vi}$ [mm]
$Y_d$ dimensional vertical distance [mm]
$Y_T$ $Y_d - Y_{ti}$ [mm]
$Y_{ti}$ vertical location of temperature interface [mm]
$Y_{vi}$ vertical location of velocity interface [mm]
$Y_{vm}$ vertical location in the outer region where $U = 0.5U_m$ [mm]
$Y_{vmax}$ vertical location of maximum velocity [mm]
$Y_{vmin}$ vertical location of minimum velocity [mm]

*Greek symbols*
$\alpha$ coefficient of thermal expansion [1/°C]
$\beta$ coefficient of solutal contraction [1/wt.%]
$\delta_{bot} = (\delta_T)_{bot} - (\delta_C)_{bot}$ the thickness of the layer with positive density gradient below the interface [mm]
$\delta_C$ the thickness of the inner concentration gradient layer [mm]
$\delta_T$ the thickness of the inner temperature gradient layer [mm]
$(\delta_C)_{bot}$ the thickness of the inner concentration gradient layer below the center of the interface [mm]
$(\delta_T)_{bot}$ the thickness of the inner temperature gradient layer below the center of the interface [mm]
$\delta_m$ $|Y_{vm} - Y_{vi}|$ [mm]
$\delta_{05}$ total interface thickness [mm]
$\kappa$ coefficient of heat diffusivity [mm$^2$/s]
$\nu$ kinematic viscosity [mm$^2$/s]

Tanny and Tsinober [3,4], Schladow et al. [5] and Kranenborg and Dijkstra [6]. While the above studies mainly considered the two-dimensional nature of the problem, Chan et al. [7] have recently explored three-dimensional effects in convection layers generated by lateral heating of a linear solute profile.

Evidently, the merging process is controlled by the conditions at the interface separating the layers. Consequently, several research works were focused on the behavior of a single salinity interface in a laterally heated fluid. Bergman and Ungan [8] studied experimentally the behavior of a two-layer system destabilized by lateral heating and cooling in a box. They pointed out that the interface is simultaneously exposed to shear instability due to the co-rotating circulation in each layer, and to double-diffusive instability due to the stabilizing and destabilizing vertical solute and temperature gradients, respectively. Using the liquid-crystal flow visualization technique, they observed waves, which might have been induced by shear instability at the interface, and a central vortex, just before the system was completely mixed. Using the shadowgraph technique Kamakura and Ozoe [9] were able to observe the appearance of waves at the interface, followed by rapid mixing of the two layers. In their experiments, as well as in the experiments by Bergman and Ungan [8], the interface was observed to migrate upwards with time.

Nishimura et al. [10] studied the above phenomenon in three enclosures of different sizes, but of fixed aspect ratio (height/width) of $A_r = 1.25$ and depth of 170 mm. Using laser-induced fluorescence and particle paths visualization techniques, they were able to observe vortices within the interface and its tilting before the complete mixing of the system. They also reported the mixing time of the system in terms of the different physical parameters that govern the flow. The mixing time increased with

the initial concentration difference between the two layers and decreased with increasing the lateral temperature gradient. In a later study, Nishimura et al. [11] used liquid-crystal particles and the Rhodamine B dye to study the flow structure at the interface. They observed traveling plumes that ascend and descend from above and below the interface into the mixed layers. The plumes exhibited a three-dimensional flow structure. Measurement showed that the spacing (in the span-wise direction) and frequency of the plumes decrease and increase, respectively, nearly linearly with the lateral temperature difference. Nishimura et al. [12] also studied the solute transfer across the interface using a conductivity–temperature sensor especially developed for that study. The Sherwood number (the non-dimensional mass transfer coefficient) was found to increase with the lateral *Ra* number and to decrease with the buoyancy ratio.

Tanny and Yakubov [13] carried out an experimental study in which the stability of the flow adjacent to the interface was examined and the associated mixing time of the two-layer system was measured. Their study revealed that the interfacial flow can be stable or unstable and the stability criterion was determined experimentally in terms of the governing parameters of the problem. Using the schlieren flow visualization technique, they showed that under unstable conditions the flow was characterized by the existence of vortices, moving along the interface above and below it (see Fig. 3 below). On the other hand, under stable conditions no vortices were observed.

All the above studies considered the case in which the two layers were of equal depth. Recently, Tanny and Yakubov [14] studied the effect of variable layer-depth ratio on the time until complete mixing of the system is reached. They found strong effect of the initial layer-depth ratio on the mixing time.

From the above review it appears that in the existing literature various mechanisms are suggested for the instability and mixing processes of the two-layer stratified fluid. These mechanisms include: vortices within or outside the interface; waves or plumes at the interface; interface migration and penetration of wall boundary layers (as was observed by Tanny and Yakubov [13], see their Fig. 6). The experimental stability analysis by Tanny and Yakubov [13] clearly indicated that the appearance of vortices above and below the interface considerably shortened the mixing time of the system by enhancing the solute transport across the interface.

Still, the mechanism that dominates the onset of interfacial instability and the consequent appearance of vortices, plumes or waves was not identified. As yet, it is not known whether it is the velocity shear across the interface, the velocity shear above and below it (as would be implied by the observations of vortices or plumes moving above and below the interface [12–14]), the opposing temperature and concentration gradients across the interface which are conducive to thermal or double diffusive convection, or some combination of all these mechanisms. As a first step to elucidate this issue and to enable a future stability analysis of the interface, we report in this paper on detailed measurements of the structure of the flow, namely, we present the velocity field and the temperature and concentration profiles at and around the interface. Also presented are some characteristics of the flow stability derived from spectral analysis of the velocity field and a series of temperature and concentration profiles measured under a variety of physical conditions. A possible instability mechanism is finally discussed.

## 2. Experimental set-up and procedures

The experiments were carried out in a box (see Fig. 1) with inner length, width and height dimensions of 100, 100 and 92 mm, respectively. Two sidewalls of the box were made of stainless steel and were provided with passages through which water from two constant-temperature baths could circulate. The two other sidewalls were made of optical glass to facilitate schlieren flow visualization and PIV measurements. The metal sidewalls and the top and base of the box were insulated using Styrofoam plates. The optical glass sidewalls were insulated by transparent thermal insulation units, each consisting of air-filled, optical glass box. The temperature of each sidewall was measured by 5 miniature thermocouples type T, inserted into holes from the backside of the metal wall.

The flow was visualized using a schlieren system (Fig. 1b) consisting of two spherical mirrors, 15.24 cm in diameter and 152.4 cm in focal length, a white light source and a knife-edge. The system was set up such that the parallel beam was passed horizontally through the optical windows of the tank. The output of the schlieren system was imaged by a video camera and recorded by a VCR for later reviewing.

Vertical concentration and temperature profiles were measured by a micro-scale conductivity/temperature instrument (MSCI, Precision Measurement Engineering, CA, USA). The sensor was traversed vertically through the stratified fluid (Fig. 1a) using a traversing system. Readings at a sampling rate of 100 Hz were done at each station over a period of 10.24 s. Data were always recorded while the probe was traversed downwards, with the sensor ahead of the probe holder, to minimize any disturbance at the measured region. The measurements were done at the center of the box, i.e., at a distance of 50 mm from the cool and warm sidewalls. The MSCI was calibrated before each experiment against an aqueous solution of the maximum concentration and against

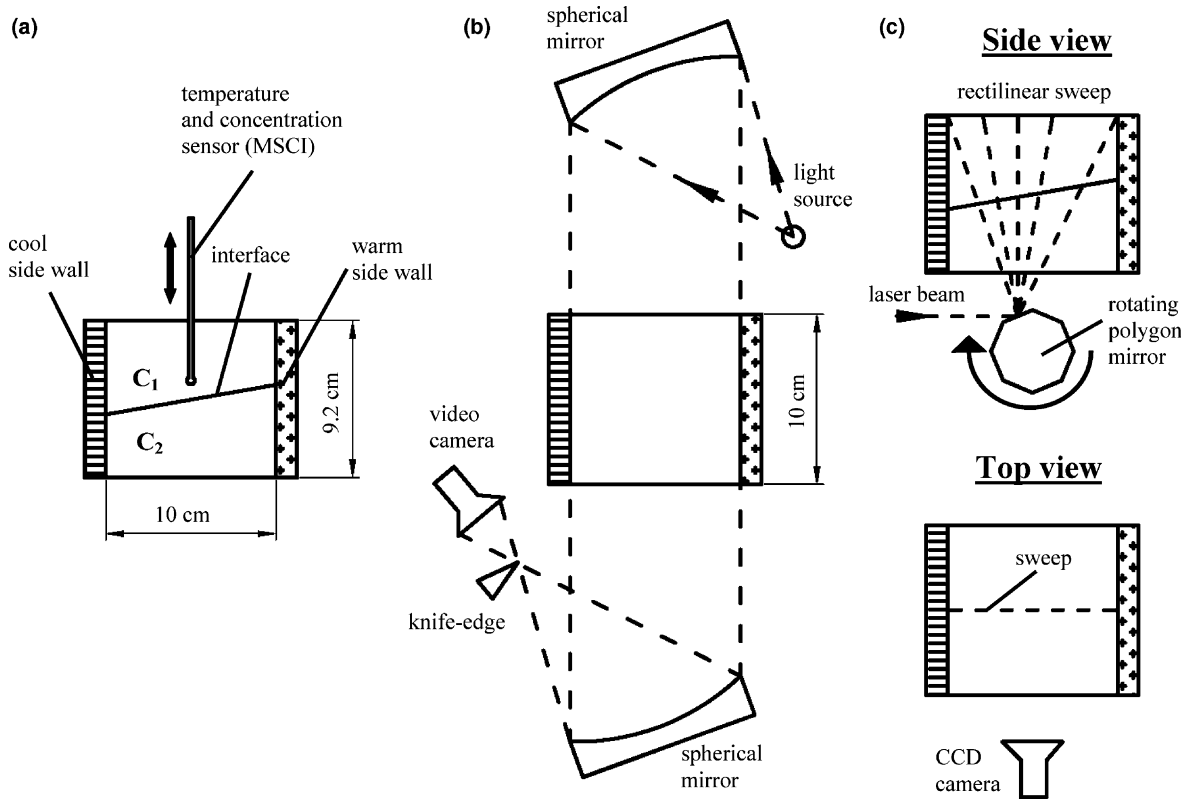


Fig. 1. Schematic views of the experimental apparatus. (a) Side view of the box with the temperature/concentration (MSCI) sensor. $C_1$ and $C_2$, represent the different concentrations of the two layers. (b) Top view of the box and the schlieren visualization system. (c) Side and top views of the box illustrating the PIV system.

two different temperatures covering the expected temperature range of the experiment. The output voltage of the sensor was translated to concentration using the local measured temperature and the relations for aqueous NaCl solutions given by Head [15].

Velocity field measurements were carried out using the PIV (Particle Image Velocimetry) technique. A laser light sheet was passed through the transparent bottom of the box illuminating the vertical mid-plane, normal to the heated and cooled sidewalls (Fig. 1c). For that purpose a thin slit was made in the bottom insulating Styrofoam plate. The light sheet was produced by deflecting a shuttered Argon-ion laser beam on a rotating polygon mirror (whose speed was computer controlled) so that it would trace a rectilinear sweep, 1.5 mm thick, over the region of interest. The illuminated plane was imaged from the side on a double frame cross-correlation CCD camera. Each pair of high-intensity sweeps exposed two individual frames, which were subsequently processed with a cross-correlation algorithm to produce vector maps of the flow field. The actual field of view of the PIV system was a rectangle of approximately 22 mm height and 16 mm width. Each sample set consisted of 200 images taken during a total sampling time of 200 s (1 Hz sampling rate). The PIV experiments utilized 10–20 μm silver-coated hollow glass spheres, which on average are slightly heavier than pure water and have a density that increases with particle diameter. An estimate of the error induced on the PIV measurements by the variation of the refractive index inside the interface is briefly discussed in Appendix A.

The two-layer stratified system was established by initially preparing two aqueous salt (NaCl) solutions of the prescribed concentrations in two separate beakers and seeding each of them with the glass spheres. Particles with density different from that of the corresponding solution were either settled down or floated up and eventually removed from the beakers.

The tank was first filled with the lower layer of aqueous solution of the higher concentration. Then, the upper layer of the lower concentration was poured carefully on the lower one (using a wooden float). The two layers had the same depth of 46 mm. After filling the tank, the system was allowed to rest for about 5 min before the start of the experiment.

In most experiments, the prescribed wall temperatures were set in advance in the two circulation baths. To start an experiment, the lateral temperature difference was applied almost instantaneously by opening valves that allow the bath fluid to circulate into the passages of the sidewalls. Apart from an initial short transient period of about 3 min, the temperature difference was almost constant throughout the experiment. The temperature of each sidewall was found to be uniform within ±0.25 °C. In part of the experiments the temperature difference between the sidewalls of the enclosure was increased stepwise with time, from 3 °C up to 24 °C, by adjusting the temperatures of the circulating baths. After each temperature adjustment the flow was allowed to reach quasi-equilibrium during a period of about 15 min and at each quasi-equilibrium state, temperature and concentration profiles were measured using the MSCI.

Due to technical constrains, it was impossible to simultaneously measure the velocity field with the PIV system and the concentration and temperature profiles with the MSCI sensor. Therefore some experiments were conducted twice, once using the MSCI along with schlieren flow visualization and once using the PIV. Earlier experience [13,14] proves that very good repeatability is obtained with this apparatus under similar controlling parameters, namely, the sidewalls temperatures and the solute concentrations of the two layers.

## 3. Results and discussion

### 3.1. Non-dimensional parameters

Before describing the experimental results, we introduce the main non-dimensional parameters associated with the flow under study. The lateral temperature difference, $\Delta T$, between the enclosure's sidewalls is represented by the thermal Rayleigh number:

$$Ra = \frac{g\alpha \Delta T L^3}{\nu\kappa}, \tag{1}$$

where $g$ is the acceleration due to gravity, $\alpha$ is the coefficient of thermal expansion, $L$ is the box length (distance between warm and cool side walls, see Fig. 1a), $\nu$ is the kinematic viscosity and $\kappa$ is the coefficient of thermal diffusion. The ratio between the stabilizing effect of solute concentration difference and the destabilizing effect of the lateral temperature difference is represented by the overall buoyancy ratio:

$$R_\rho = \frac{\beta \Delta C}{\alpha \Delta T}, \tag{2}$$

where $\beta$ is the coefficient of solutal contraction and $\Delta C = C_2 - C_1$ (see Fig. 1a) is the concentration difference between the two layers. A local buoyancy ratio across the interface is defined as:

$$R_{\rho \mathrm{l}} = \frac{\beta \Delta C}{\alpha \Delta T_\mathrm{i}}, \tag{3}$$

where $\Delta T_\mathrm{i}$ is the local vertical destabilizing temperature difference across the interface.

The geometry of the problem is governed by the aspect ratio of the box, $A_\mathrm{r} = H/L$, where $H$ is the depth of the fluid. The present experiments were carried out with two layers of equal thickness (46 mm each) such that $H = 92$ mm and $A_\mathrm{r} = 0.92$.

The dimensional frequency of the velocity disturbance, $f$, is represented in a non-dimensional form by the Strouhal number:

$$St = \frac{f \delta_\mathrm{m}}{U_\mathrm{m}}, \tag{4}$$

where $\delta_\mathrm{m}$ is the vertical distance between $Y_\mathrm{vi}$, the center of the velocity interface, and $Y_\mathrm{vm}$, the vertical location in the outer region where $U = 0.5U_\mathrm{m}$. (A more detailed definition of $Y_\mathrm{vi}$ and $Y_\mathrm{vm}$ is given in Section 3.2.1). $U_\mathrm{m}$ is defined as the maximum absolute value of the mean horizontal velocity, either above or below the interface.

The physical properties of the fluid were estimated at the mean temperature and concentration in the system, using the data given in Ruddick and Shirtcliffe [16] and Weast [17].

### 3.2. The velocity field

#### 3.2.1. The mean velocity profile

Fig. 2a shows the vertical profile of mean horizontal velocity as measured by the PIV system in an experiment with initial $\Delta C = 0.08\%$, $\Delta T = 2.04$ °C, which correspond to $Ra = 4.12 \times 10^7$ and $R_\rho = 1.04$. These conditions correspond to stable interfacial flow [13] and indeed no vortices are observed by the schlieren technique in this experiment. The profile shows counter flow with strong shear across the interface in between two opposite local maxima (inner region). The velocity decays to zero further away from it (outer region). Positive mean velocity is associated with flow from the cool to the warm sidewall. We define the velocity interface location ($Y_\mathrm{vi}$) as the point of zero velocity, obtained by fitting a linear curve (solid straight line in Fig. 2a) to the measured points within a suitable interval. The end points of this interval correspond to the positions where the local velocity $U = 0.5(U_\mathrm{max} + U_\mathrm{min}) \pm 0.15(U_\mathrm{max} - U_\mathrm{min})$, where $U_\mathrm{max}$ and $U_\mathrm{min}$ are respectively, the maximum and minimum values of the velocity profile. Note that the level of $Y_\mathrm{vi}$ almost coincides with the vertical center of the PIV image, $Y_\mathrm{d} = 0$. The maximum (minimum) velocity is obtained by fitting a parabola (solid curved lines in Fig. 2a) to the experimental data points, surrounding the measured maximum (minimum)

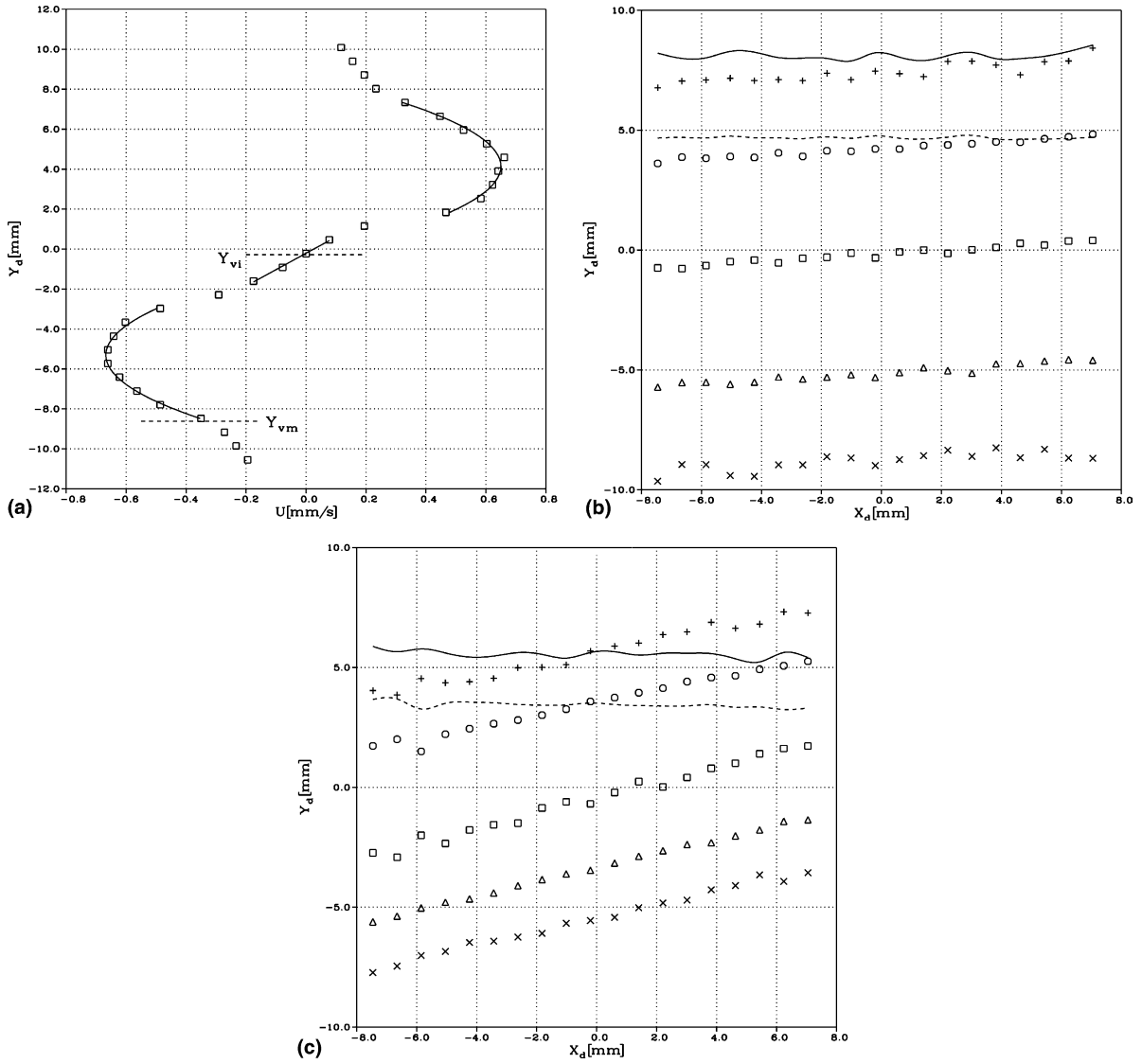


Fig. 2. (a) The vertical profile of mean horizontal velocity at the interfacial region at $t = 15$ min. The structure of the interface is shown at (b) $t = 15$ and (c) $t = 72$ min after the start of the experiment. (b) and (c) show the location of the interface (squares), locations of velocity maxima above (circles) and below (triangles) the interface, half of the distance between the locations of velocity maxima (broken line), the locations at the outer parts where the velocity equals half of its maximum or minimum (plus and cross symbols, respectively) and half of the distance between the two latter locations (solid line).

velocity above (below) the interface. The corresponding locations where the velocity attains its maximum and minimum values on each side of the interface, respectively, ($Y_{vmax}$, $Y_{vmin}$) separate the inner and outer regions of the velocity interface.

Fig. 2b and c (for $t = 15$ and 72 min, respectively, where $t$ is the time elapsed from the start of the experiment) illustrate graphically the interface structure of two flow fields measured in consecutive times in the above experiment. The horizontal ($X_d$) and vertical ($Y_d$) axes represent the field of view of the CCD camera, where $X_d = Y_d = 0$ is the center of the PIV image which corresponds to the center of the box mid cross section. In each figure we observe the location of the interface ($Y_{vi}$, square symbols), the locations of the velocity maxima above ($Y_{vmax}$, circles) and below ($Y_{vmin}$, triangles) the interface, the distance between the locations of velocity maxima ($Y_{vmax} - Y_{vmin}$, broken line), the locations at the outer parts away from the interface, obtained by linear interpolation, where the velocity equals half of its maximum or minimum ($Y_{vmax05}$, $Y_{vmin05}$, the plus and cross symbols above and below the interface,

respectively) and the distance between the two latter locations ($\delta_{05,}$ solid line). The distance $Y_{vmax} - Y_{vmin}$ represents the inner layer thickness, whereas the total interface thickness is associated with $\delta_{05}$.

In Fig. 2b, taken at a relatively early stage of the experiment, the interface is slightly tilted. The inner layer thickness (broken line) is about 9.5 mm whereas the total interface thickness (solid line) is about 16 mm. Note that for illustrative purposes half of the total interface thickness ($\delta_{05}/2$) and half of the inner layer thickness ($(Y_{vmax} - Y_{vmin})/2$) are presented in Fig. 2b and c. Fig. 2c, taken at a later stage of the same experiment, illustrates the sharp tilt (inclination of about 12°) of the interface (square symbols). In spite of this sharp tilt, the total interface thickness and the inner layer thickness are nearly uniform along the horizontal. The interface becomes thinner with time, with $Y_{vmax} - Y_{vmin} \approx 7$ mm and $\delta_{05} \approx 11$ mm.

### 3.2.2. Spectral analysis

Spectral analysis is carried out of the instantaneous velocity profiles, measured in an experiment with $\Delta C = 0.56\%$, $\Delta T = 22.52$ °C, which correspond to $Ra = 4.46 \times 10^8$ and $R_\rho = 0.66$. These conditions correspond to unstable interfacial flow [13] and vortices are observed by the schlieren technique in this experiment.

The present schlieren images (see an example in Fig. 3), as well as the photographs of Tanny and Yakubov [13] show that the vortices move above and below the interface, in a direction associated with the convective circulation in each layer, i.e., the vortices above the interface move from the cool to the warm sidewall and those below it from the warm side wall to the cool one. However, the vortices are not generated immediately at the cool or warm sidewall but at some distance from it. Fig. 3 shows that at their generation the vortices are relatively small but while moving along the interface, they gradually grow in size until they hit the opposite cool/warm sidewall.

Thus at the interface and along the horizontal direction, a region may be found where vortices exist below the interface but not above it (e.g., near the cool sidewall, Fig. 3), and vice versa. This raises the possibility that the instability associated with one side of the interface only weakly depends on that of the other side. On the other hand, away from the sidewalls, at the middle of the box, Fig. 3 suggests that vortices exist simultaneously on both sides of the interface. To check this possibility, spectral analysis of the time dependent velocity field measured across the interface near the cool sidewall as well as at the middle of the box, is carried out.

Fig. 4a shows the vertical profiles of mean horizontal ($U$, squares) and vertical ($V$, circles) velocities, measured across the interface near the cool sidewall. Both mean velocities are normalized by $U_m$. The normalized depth, $Y/\delta_m$ (vertical axis) is measured above or below the center of the velocity interface, $Y_{vi}$ where $Y = Y_d - Y_{vi}$. The associated averaged power spectra obtained from a set of instantaneous velocity measurements, above and below the interface, are shown in Fig. 4b and c, respectively, as a function of the Strouhal number, $St$. The solid and dash lines are the normalized power spectra of the vertical ($v$) and horizontal ($u$) velocity components, respectively. The averaged power spectra are calculated by averaging the local spectra over all measurements positions above or below the velocity interface location ($Y_{vi}$). The maximum power obtained from the $u$ and $v$ spectra is used to normalize both.

A significant difference between the shape of the horizontal mean velocity profile above and below the interface is observed (Fig. 4a). This profile corresponds to the region near the cool sidewall. The flow above the interface has just arrived from the cool sidewall and consists of flow without vortices, characterized by a relatively narrow "nose". On the other hand, the flow below the interface arrives from the opposite warm sidewall and is already developed, consisting of vortices which make

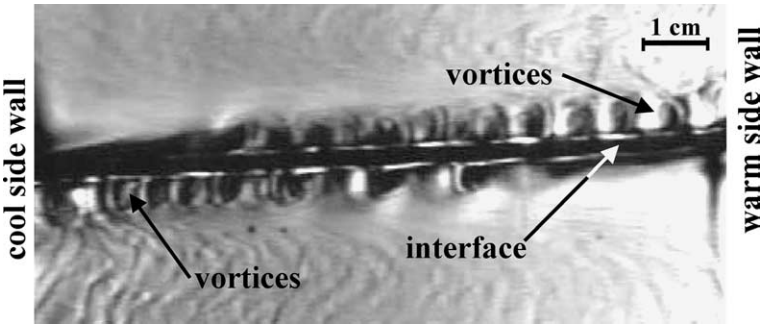


Fig. 3. A schlieren image of the vortices at the interface. Experimental conditions are: $Ra = 4.46 \times 10^8$, $R_\rho = 0.66$. The vortices above the interface move towards the warm sidewall while the vortices below the interface move towards the cool sidewall. The motion of the vortices is caused by the circulating flow within each layer.

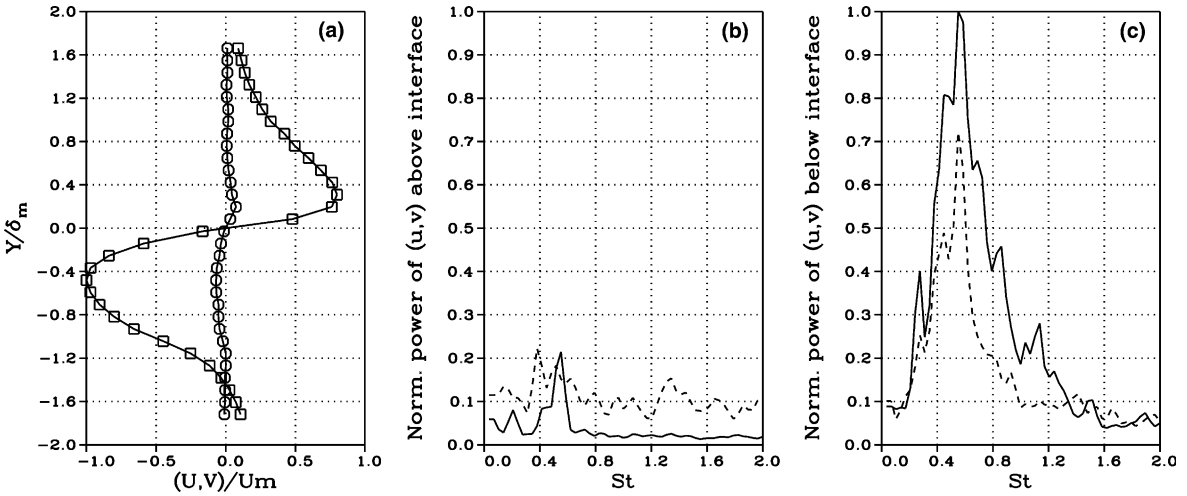


Fig. 4. (a) Vertical profiles of the mean horizontal (squares) and vertical (circles) velocities (normalized by the maximum absolute value of the horizontal mean velocity) for $Ra = 4.46 \times 10^8$, $R_\rho = 0.66$, $t = 72$ min, near the cool sidewall. (b) Normalized average power spectrum of the horizontal (dashed line) and vertical (solid line) velocity perturbations above the interface as a function of the $St$ number. (c) Normalized average power spectrum of the horizontal (dashed line) and vertical (solid line) velocity perturbations below the interface as a function of the $St$ number. $U_m = 1.38$ mm/s; $\delta_m = 6.06$ mm.

the velocity "nose" much thicker than that above the interface, due to the enhanced mixing.

The above observations are reflected by the power spectra corresponding to the regions above (Fig. 4b) and below (Fig. 4c) the interface. While the spectra above the interface are almost uniform, the spectra below the interface show significant amplification of energy over a wide band of $St$ (0.2–1.3, corresponding to the frequency range 0.05–0.3 Hz) with a distinct peak at about $St = 0.57$ ($f = 0.13$ Hz). Although the magnitude of the mean vertical velocity is much lower than that of the mean horizontal component, their associated power spectra shapes (below the interface) are very similar and their magnitudes are about the same, indicating the existence of coherent vortices in this region.

To further illustrate the correlation between the observation of vortices by the schlieren technique and the power spectrum, the latter is also calculated for an experiment conducted under stable conditions ($\Delta C = 0.08\%$, $\Delta T = 2.04$ °C, which correspond to

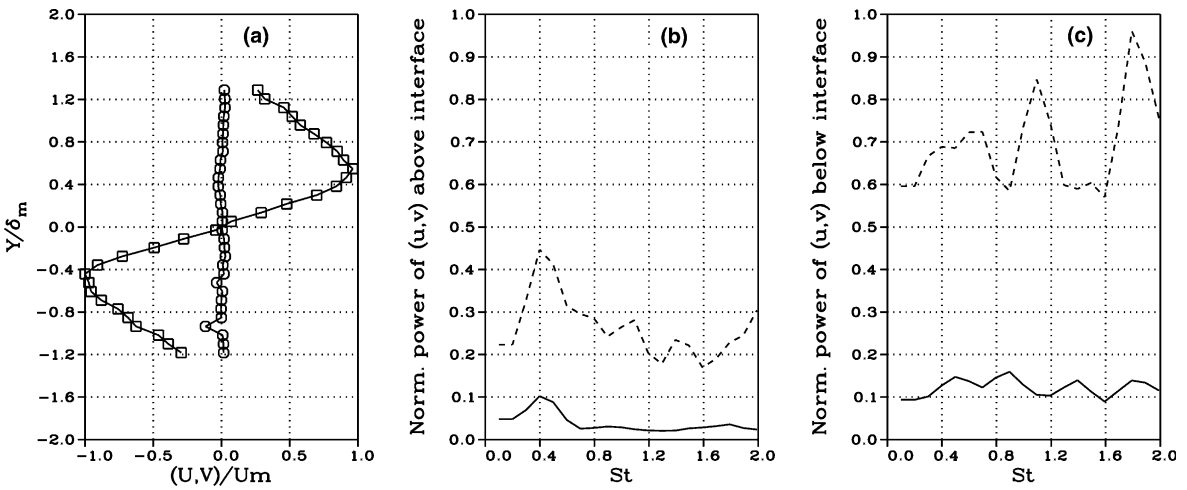


Fig. 5. (a) Vertical profiles of the mean horizontal (squares) and vertical (circles) velocities (normalized by the maximum absolute value of the horizontal mean velocity) for $\Delta C = 0.08\%$, $\Delta T = 2.04$ °C, which correspond to $Ra = 4.12 \times 10^7$ and $R_\rho = 1.04$. (b) Normalized average power spectrum of the horizontal (dashed line) and vertical (solid line) velocity perturbations above the interface as a function of the $St$ number. (c) Normalized average power spectrum of the horizontal (dashed line) and vertical (solid line) velocity perturbations below the interface as a function of the $St$ number. $U_m = 0.66$ mm/s; $\delta_m = 8.35$ mm.

$Ra = 4.12 \times 10^7$ and $R_\rho = 1.04$ and the mean flow shown in Fig. 2a) where no vortices were observed both above and below the interface. Fig. 5, which follows the same structure of Fig. 4, shows the mean velocity profiles (5a), and the normalized power spectra above (5b) and below (5c) the interface. While in the case where vortices exist (see the spectrum of $v$, Fig. 4c) the ratio between peak to noise is about 17, in Fig. 5b, without vortices, this ratio is only about 3. Thus the spectra plots are in accordance with the schlieren images, which do not show vortices under these stable conditions.

Figs. 6–8 follow the same structure as that of Figs. 4 and 5, except for the fact that only the power spectra of the vertical velocity are presented. These results are obtained from PIV data acquired at the same experiment as Fig. 4 but at the middle of the box, approximately in between the cool and warm sidewalls. Figs. 6–8 show results at distances of 43.33 mm, 48.14 mm and 56.14 mm, respectively, from the warm sidewall (recall that the center of the PIV image coincides with the enclosure's horizontal center, 50 mm from each sidewall).

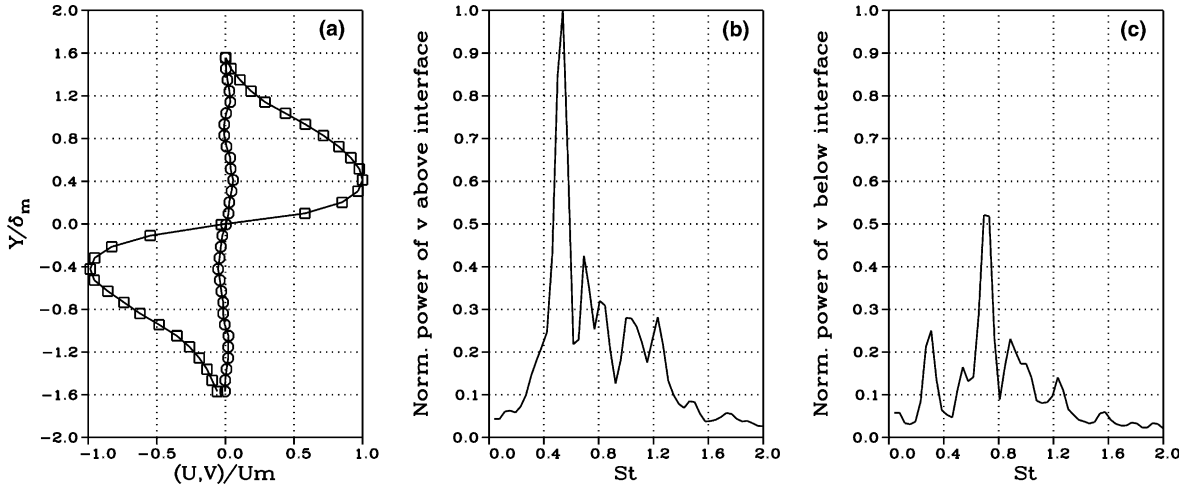


Fig. 6. (a) Vertical profiles of the mean horizontal (squares) and vertical (circles) velocities (normalized by the maximum measured horizontal mean velocity) in an experiment with $Ra = 4.46 \times 10^8$ and $R_\rho = 0.66$, at $t = 18$ min. The profiles are measured 43.33 mm from the warm sidewall. (b) Power spectrum of $v$ above the interface. (c) Power spectrum of $v$ below the interface. $U_m = 1.34$ mm/s; $\delta_m = 6.55$ mm.

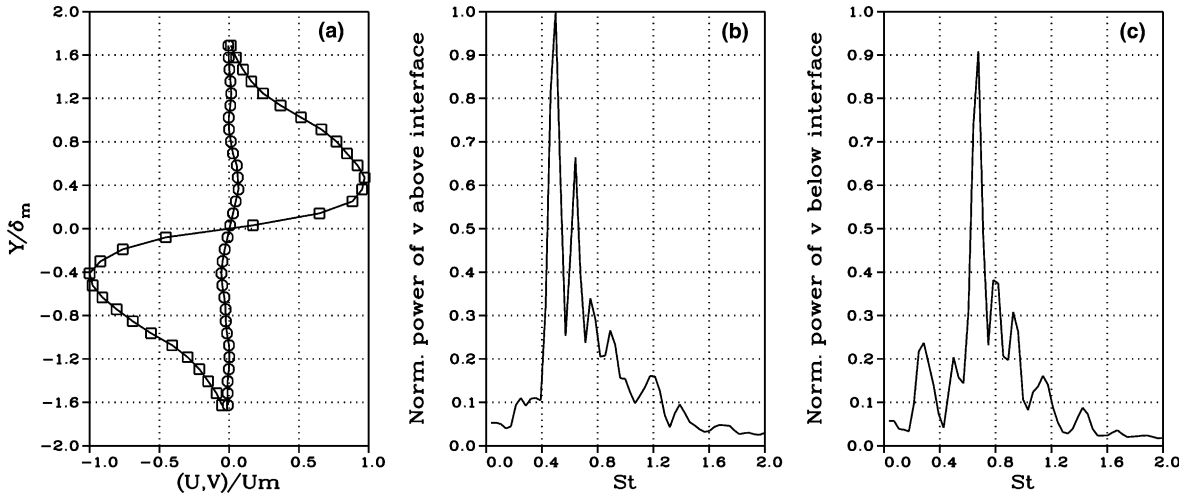


Fig. 7. Same as Fig. 6 but for profiles measured 48.14 mm from the warm sidewall. $U_m = 1.37$ mm/s; $\delta_m = 6.18$ mm.

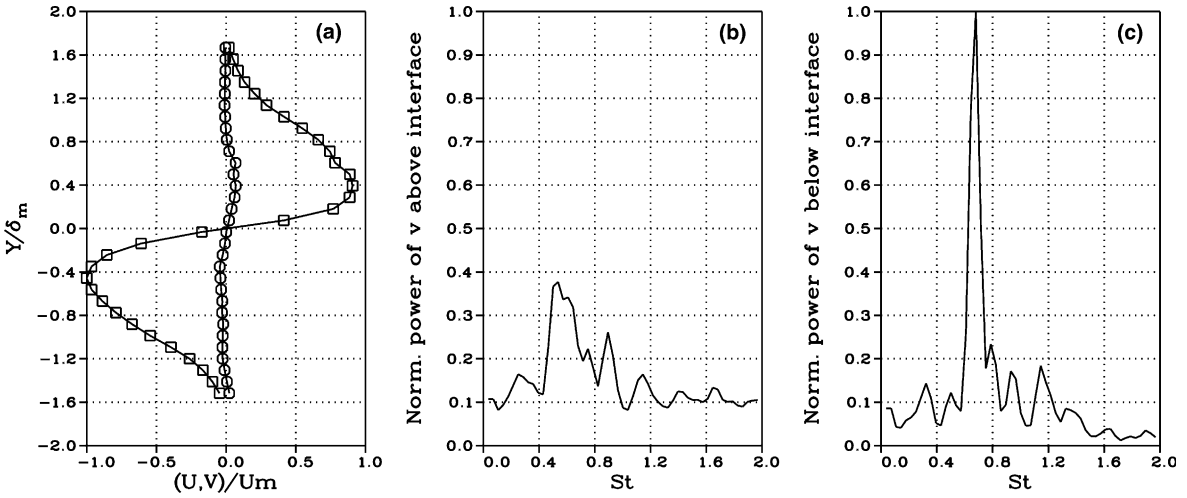


Fig. 8. Same as Fig. 6 but for profiles measured 56.14 mm from the warm sidewall. $U_m = 1.42$ mm/s; $\delta_m = 6.43$ mm.

The series of the three figures shows that the dominant frequency above the interface is about 0.11 Hz ($St = 0.54$, 0.5 and 0.5 in Figs. 6–8 respectively) whereas below the interface it is about 0.15 Hz ($St = 0.73$, 0.68 and 0.68 in Figs. 6–8 respectively). It is clear that in the region, which is slightly closer to the warm sidewall, the energy peak above the interface (6b) is larger than that below it (6c). At the intermediate region the two peaks, above (7b) and below (7c) the interface, have about the same value and in the region slightly closer to the cool sidewall the spectrum peak below the interface (8c) is significantly larger than that above it (8b). It should be noted that the frequency of 0.15 Hz has also considerable amount of energy above the interface (Fig. 7b). These results support the schlieren observation (Fig. 3) that the vortices grow as they travel towards the warm (cool) sidewall above (below) the interface.

The vertical distributions of the normalized power of $u$ and $v$ at the dominant frequencies of 0.15 Hz and 0.11 Hz (corresponding to $St$ numbers of 0.68 and 0.5 respectively) are shown respectively in Figs. 9 and 10. Each figure consists of three parts: the vertical profiles of the normalized mean horizontal ($U$, squares) and vertical ($V$, circles) velocities are shown in (a) and the

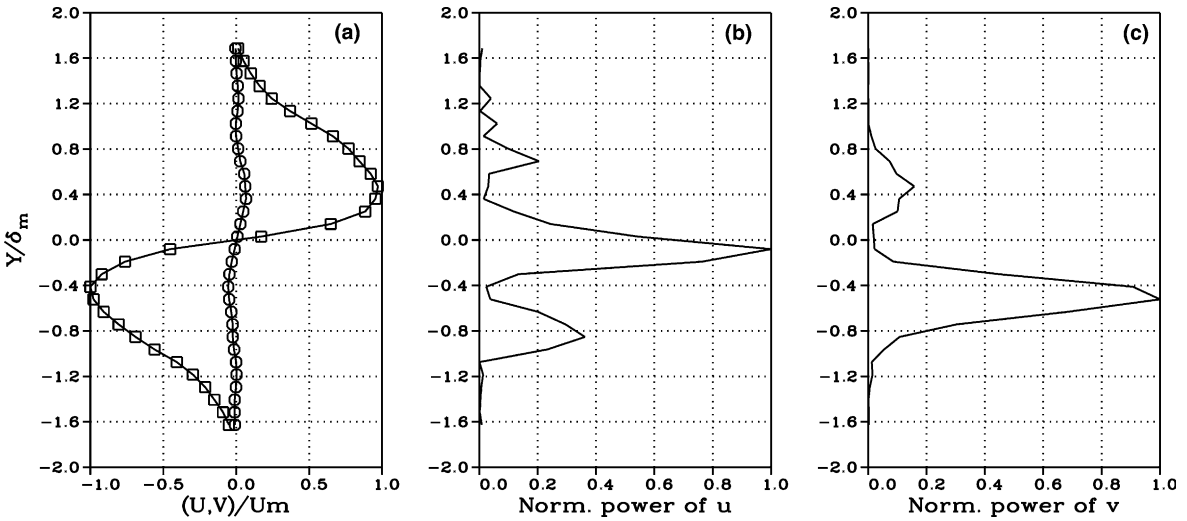


Fig. 9. (a) Vertical profiles of the mean horizontal (squares) and vertical (circles) velocities (normalized by the maximum measured horizontal mean velocity) in an experiment with $Ra = 4.46 \times 10^8$, $R_\rho = 0.66$, $t = 18$ min. The profiles are measured 48.14 mm from the warm sidewall. Frames (b) and (c) are vertical distributions of the normalized power of $u$ and $v$, respectively, at the dominant frequency of $f = 0.15$ Hz ($St = 0.68$). $U_m = 1.37$ mm/s; $\delta_m = 6.18$ mm.

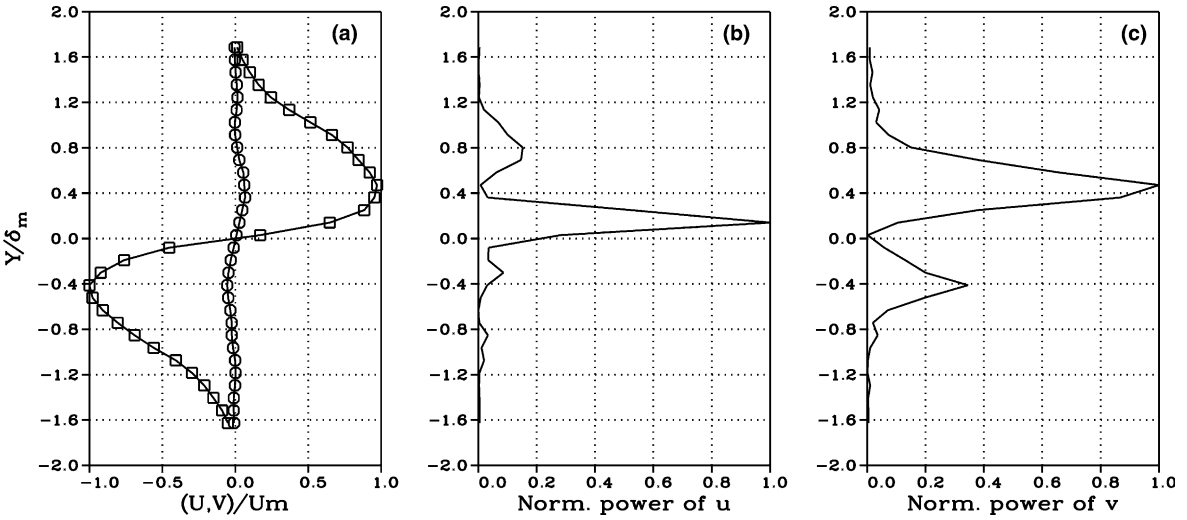


Fig. 10. Same as Fig. 9, with power spectra calculated at $f = 0.11$ Hz ($St = 0.5$). $U_m = 1.37$ mm/s; $\delta_m = 6.18$ mm.

normalized powers of $u$ and $v$ are shown respectively in (b) and (c). It can be seen that the shape of the power distributions associated with one of the frequencies is almost a mirror image of the other: the power of the lower frequency (0.11 Hz, Fig. 10) is dominant above the interface whereas the power of the higher frequency (0.15 Hz, Fig. 9) prevails below the interface. The primary and secondary peaks of the $u$ perturbation are located within the inner and outer regions of the velocity interface, respectively. The vertical positions of the peaks of the $v$ perturbation correspond approximately to the minima of the $u$ perturbation as well as to the maximum and minimum of the mean horizontal velocity.

### 3.3. Concentration and temperature profiles

In Fig. 11 we illustrate the structure of the flow through an example of velocities, concentration and temperature profiles measured under conditions of $Ra = 4.46 \times 10^8$ and $R_\rho = 0.66$ (unstable interfacial flow

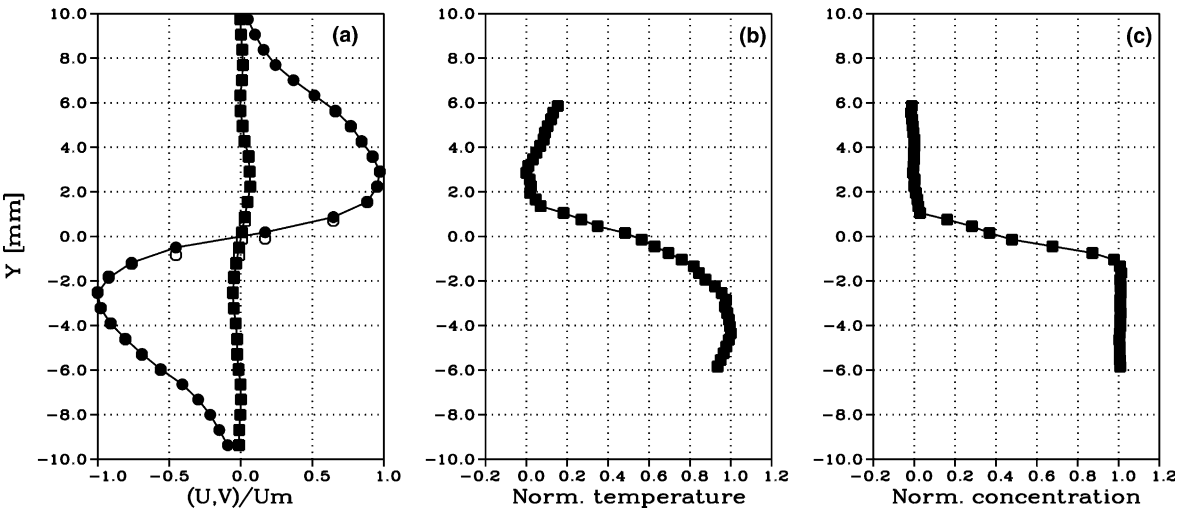


Fig. 11. The structure of the interface. (a) Vertical profiles of the mean horizontal (circles) and vertical (squares) velocities (normalized by the maximum measured horizontal mean velocity) in an experiment with $Ra = 4.46 \times 10^8$, $R_\rho = 0.66$, $t = 18$ min. Black-filled symbols are measured values and open symbols are values corrected for optical distortion. Vertical profiles of normalized temperature (b) and concentration (c) for similar conditions as (a). Temperature and concentration are normalized by their corresponding maximum differences across the interface.

with vortices). The vertical axis in each figure (a–c) is $Y = Y_d - Y_{vi}$. (Note that the vertical center of the concentration interface is slightly shifted). Black-filled symbols are measured values and open symbols are values corrected for optical distortion (for more details see Appendix A).

It can be seen that the thickness of the inner velocity layer (Fig. 11a) is approximately equal to that of the inner temperature layer (Fig. 11b), and both are about twice that of the inner concentration layer (Fig. 11c). Outside the inner stabilizing concentration layer but within the inner velocity and temperature layers, (approximately within the ranges $-3 < Y < -1.5$ and $1.5 < Y < 3$) the concentration on each side of the interface is almost uniform, whereas the temperature has a destabilizing effect which may induce instability phenomena at these regions. On the other hand, at the outer velocity regions, due to the inflection points in the outer parts of the horizontal velocity profile (at about $Y = \pm 7$ mm), the velocity profile may have a destabilizing effect. However, in these outer regions on both sides of the interface, the temperature increases monotonically with height and consequently stabilizes the flow. These observations support the schlieren visualization of the formation of vortices adjacent to the interface on each side of it (Fig. 3).

The above observation suggests that regions of positive density gradient (hydrostatic instability), caused by the combination of a uniform concentration profile and a negative temperature gradient are associated with the onset of vortices above and below the interface. Fig. 12 shows two pairs of profiles from an experiment in which the horizontal temperature difference was adjusted stepwise with time (see Section 2). Here, the vertical axis is $Y_T = Y_d - Y_{ti}$ where $Y_{ti}$ is the center of the temperature interface determined in a similar way as $Y_{vi}$. For each pair of profiles, analytical functions were fitted to the temperature and concentration data points and the vertical density gradient was calculated by

$$\frac{1}{\rho_0}\frac{d\rho}{dy} = -\alpha\frac{dT}{dy} + \beta\frac{dC}{dy}.$$

In the profiles of Fig. 12 the points where the density gradient is positive are marked by black-filled symbols. The profiles in Fig. 12a, measured when the interfacial flow was stable (no vortices), show a relatively thin region (≈1 mm) of positive density gradient below the interface. On the other hand, in Fig. 12b, which corresponds to a case of unstable interfacial flow (vortices), the region of positive density gradient below the interface is considerably thicker (≈2.5 mm). This suggests that a relatively thick region of positive density gradient is necessary for the onset of interfacial instability. Such a situation can be realized when the stabilizing concentration gradient layer is much thinner than the destabilizing temperature layer, i.e., when the ratio between the thicknesses of these two layers, $\delta_C/\delta_T$ is relatively small. The thickness $\delta_T$ is the vertical distance between the two local temperature maxima adjacent to the interface and the thickness $\delta_C$ is the vertical distance between the edges of the concentration gradient layer.

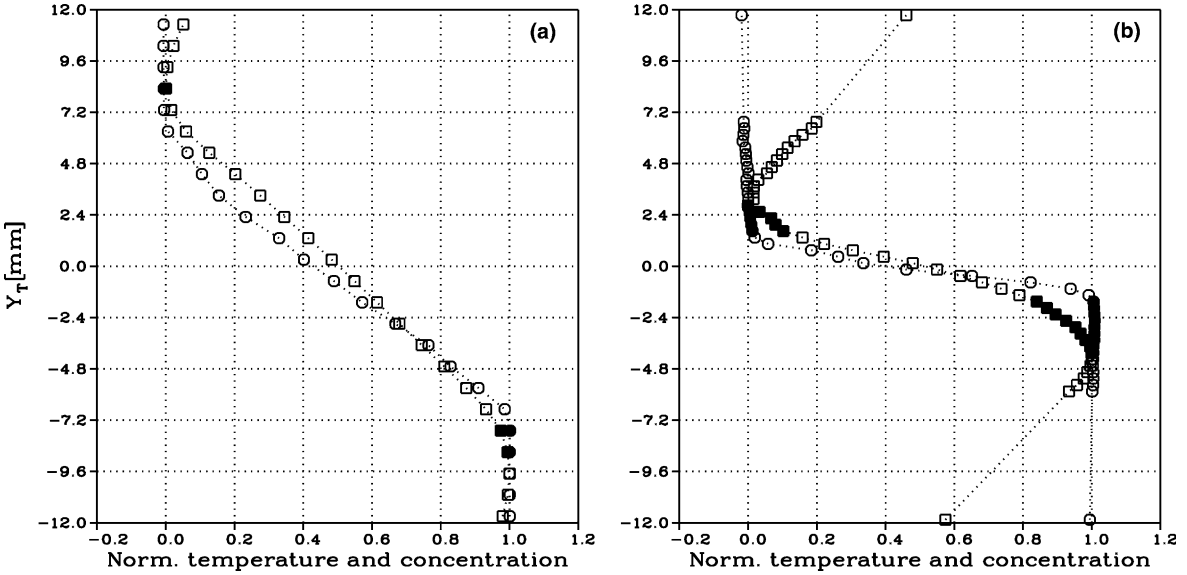


Fig. 12. Vertical concentration and temperature profiles under two different physical conditions. (a) $\Delta C = 1.08\%$, $\Delta T_i = 1.95$ °C, stable conditions (no vortices). (b) $\Delta C = 0.72\%$, $\Delta T_i = 4.61$ °C, unstable conditions (with vortices). The black-filled symbols represent hydrostatically unstable regions with a positive vertical density gradient.

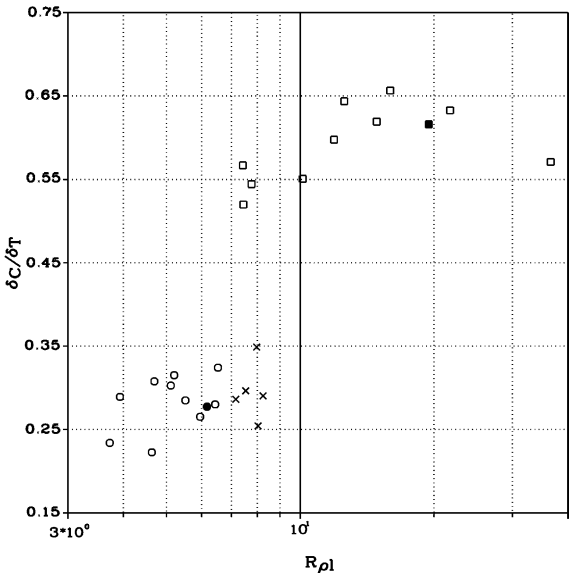


Fig. 13. The thickness ratio between the concentration and temperature gradient layers, $\delta_C/\delta_T$, as a function of the local buoyancy ratio, $R_{\rho l}$. (□) no vortices (stable); (×) faint vortices (transition); (○) vortices (unstable). The black-filled square and circle symbols correspond to the profiles of Fig. 12a and b, respectively.

The ratio between the thicknesses of the concentration and temperature layers, $\delta_C/\delta_T$ is plotted in Fig. 13 as a function of the local buoyancy ratio, $R_{\rho l}$, defined on the basis of the vertical temperature difference measured across the interface in each profile ($\Delta T_i$) and the corresponding instantaneous concentration difference between the two layers. In this experiment successively decreasing values of $R_{\rho l}$ were realized by the stepwise increase with time of the horizontal temperature difference (see Section 2) while allowing the concentration step to decrease by solute diffusion through the interface. Thus, higher values of $R_{\rho l}$ represent more stable conditions.

The data points in Fig. 13 show two distinct regimes with a sharp transition between them, at $R_{\rho l} \approx 7.5$. At relatively high values of $R_{\rho l}$, the ratio $\delta_C/\delta_T$ is high (>0.5) whereas at lower values of $R_{\rho l}$, $\delta_C/\delta_T$ is much smaller (<0.325). It is recalled that high values of $\delta_C/\delta_T$ are associated with relatively thin layers of positive density gradient resulting in a stable interfacial flow; indeed, for $R_{\rho l} > 8.5$ no vortices were observed at the interface by the schlieren technique (square symbols in Fig. 13). On the other hand, small $\delta_C/\delta_T$ corresponds to less stable conditions and the observations showed that for $R_{\rho l} < 7$ the interfacial flow was characterized by vortices (circle symbols in Fig. 13). The transition from stable to unstable interfacial flow, at $7 < R_{\rho l} < 8.5$, was characterized in most cases by faint vortices above and below the interface (× symbols in Fig. 13). The black-filled square and circle symbols correspond to the profiles of Fig. 12a and b respectively.

It is also noticed in Fig. 13 that in all cases, $R_{\rho l} > 1$, hence the whole interface is hydrostatically stable. This, however, does not preclude the existence of thinner subregions, above and below the interface, where hydrostatic instability prevails and leads to the onset of vortices. (For $R_{\rho l} < 1$, the entire interface would have become unstable leading to its breakup and complete mixing of the two layers).

The above findings suggest that the interfacial flow becomes unstable through a mechanism, which is essentially thermal and similar to Rayleigh–Bénard convection (with a weak velocity shear). As the layer with the positive density gradient becomes thicker, the value of a local Rayleigh number increases, the flow may become unstable, and transverse, two-dimensional vortices can emerge. This hypothesis is verified by considering in more detail the concentration and temperature profiles just below the interface. (Due to asymmetry, the layer of positive density gradient above the interface is considerably thinner than that below the interface resulting in much more scattered results (not shown) in this region). Fig. 14 presents the ratio between the concentration and temperature interface thicknesses for the region below the interface as a function of a local Rayleigh number, $Ra_{bot}$, defined over the layer with unstable density gradient as:

$$Ra_{bot} = \frac{g\alpha\Delta T_{bot}\delta_{bot}^3}{\nu\kappa},$$

where $\Delta T_{bot}$ is the vertical temperature difference across the layer of positive density gradient below the interface

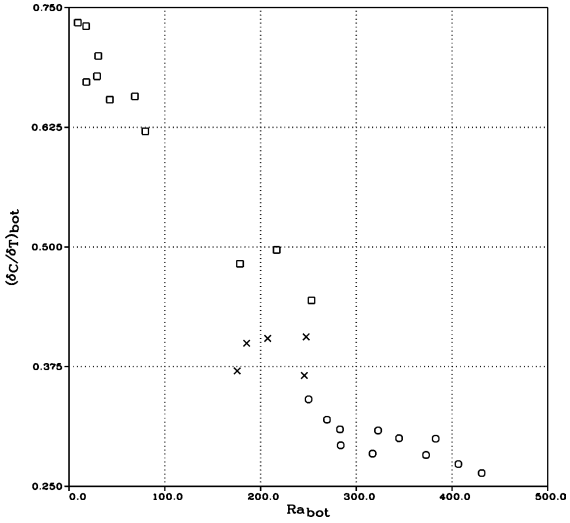


Fig. 14. The thickness ratio between the concentration and temperature gradient layers with positive density gradient below the interface, $(\delta_C/\delta_T)_{bot}$ as a function of the local Rayleigh number, $Ra_{bot}$. (□) no vortices (stable); (×) faint vortices (transition); (○) vortices (unstable).

and $\delta_{bot} = (\delta_T)_{bot} - (\delta_C)_{bot}$ is the thickness of this layer. For example, with reference to Fig. 12, $\Delta T_{bot}$ and $\delta_{bot}$ are, respectively, the temperature difference across, and the thickness of the layer below the interface which is marked with black-filled symbols. Since, at this region, the concentration is uniform with height, its contribution to the density gradient is negligible and only the thermal Rayleigh number is considered.

Fig. 14 presents a strong correlation between the stability of the interfacial flow and the value of the local Rayleigh number, $Ra_{bot}$. Low values of $Ra_{bot}$ (<170) are associated with high values of $(\delta_C/\delta_T)_{bot}$ which correspond to a stable flow (no vortices, square symbols). On the other hand, high values of $Ra_{bot}$ (>280) are associated with low values of $(\delta_C/\delta_T)_{bot}$ which correspond to unstable flow (vortices, circle symbols). The transition regime, represented in most cases by faint vortices (× symbols), corresponds to intermediate values of $Ra_{bot}$.

The hydrostatically unstable layers in which the vortices appear deviate from the fluid layers related to the classical Rayleigh–Bénard problem in two effects: they are subjected to a weak shear flow and they posses a non-linear vertical temperature profile. Thus, it is of interest to consider how these two effects influence the flow patterns at the onset of instability and the critical Rayleigh number. The stability of Couette and Poiseuille shear flows in plane channels heated from below was studied respectively by [18,19]. The results of these analyses show that for low Reynolds numbers the instability is thermal in origin. For an infinite horizontal domain, and low Reynolds numbers, longitudinal rolls with axes parallel to the direction of the mean flow are preferred. However, for Poiseuille flow in a finite domain, Luijkx et al. [20] proved experimentally that the critical Rayleigh number corresponding to finite transverse rolls (with axes perpendicular to the direction of the mean flow) must be smaller than the one corresponding to longitudinal rolls. Luijkx et al. [20] concluded that if the shear is small enough, rolls are aligned parallel to the shorter side of the channel and when the shear exceeds some critical value convection occurs in the form of longitudinal rolls. It is worth noting that in much larger Reynolds numbers (≅5400 for Poiseuille flow) the instability leads to two-dimensional Tollmien–Schlichting waves. The Reynolds number of the unstable layers in the present experiments is estimated to be of order 1, which supports qualitatively the proposed thermal instability mechanism and the observed onset of transverse vortices.

The analyses by [18,19] also showed that the shear stabilizes the flow, i.e., the critical Rayleigh number with shear is larger than its corresponding value in a quiescent fluid layer. However, due to the extremely small value of the Reynolds number in our case this effect is expected to be negligible (of the order of 1% [21]). On the other hand, for the Rayleigh–Bénard problem without shear but with a non-uniform temperature gradient, it was shown [22] that the critical Rayleigh number may be reduced relative to its value for a linear temperature profile. Moreover, Palm [23] has shown that spatial variations in viscosity, which may result from the temperature gradient, reduce the critical Rayleigh number as compared to the case of constant fluid properties. These results may explain the present rough estimate of the critical local Rayleigh number ($Ra_{bot} \approx 280$), which is smaller than 657.5, the value corresponding to a quiescent fluid layer with a linear temperature profile, constant fluid properties and stress-free surfaces.

In summary, it is shown that the governing mechanism for the instability of the interfacial flow is essentially thermal and similar to Rayleigh–Bénard convection (with a weak shear flow). The double diffusive instability mechanism does not seem to play an important role since it occurs only where the density is stably stratified, which is not realized in the hydrostatically unstable regions, above and below the interface, where vortices appear.

## 4. Concluding remarks

An experimental study was carried out on the structure of the interface in a two-layer stratified system in a laterally heated enclosure. Velocity field as well as temperature and concentration profiles measurements were carried out and the flow was visualized using the schlieren technique. The following conclusions can be drawn from this experimental study:

- The major instability mechanism causing the appearance of transverse vortices above and below the interface is essentially thermal and similar to Rayleigh–Bénard convection with weak shear. The onset of this type of instability is associated with relatively small values of the ratio between the thicknesses of the concentration and temperature interfacial layers. The double-diffusive and shear driven instability mechanisms do not seem to play an important role.
- The interface is tilted with respect to the horizontal direction whereas its thickness remains approximately constant. With time, the slope of the interface increases while its thickness decreases.
- The instability phenomena above and below the interface seem to be independent, probably due to the central stabilizing sharp concentration gradient. The mean horizontal velocity profile is not fully symmetric about the interface, and the asymmetry increases as the cool or warm sidewall is approached. Consequently, the stability characteristics are different above and below the interface as illustrated by the associated different power and frequency ($St$ number) of the dominant disturbances.

## Appendix A

Estimation is given for the errors induced on the PIV measurements by the spatial variation of the refractive index. Recently, Elsinga et al. [24] estimated the particle position error and the velocity error caused by the gradient and the second derivative of the refractive index, respectively. In our case the horizontal variations of the refractive index are much smaller than those in the vertical direction (see for example the variation in the grey level in Fig. 3) and thus the refractive index is assumed to be a function of the vertical coordinate only. Accordingly, the simplified expressions for the systematic errors in the vertical position and the vertical velocity implemented here for water are respectively:

$$\varepsilon_y = \frac{1}{2}\frac{W^2}{n_0}\frac{\mathrm{d}n}{\mathrm{d}Y},$$

and

$$\varepsilon_v = \frac{1}{2}\frac{W^2}{n_0}\frac{\mathrm{d}^2 n}{\mathrm{d}Y^2}.$$

Hence, $Y_{\text{corrected}} = Y_{\text{measured}} + \varepsilon_y$ and $V_{\text{corrected}} = V_{\text{measured}}/(1-\varepsilon_v)$. In the above expressions $W = 50$ mm is the distance between the PIV measurement plane and the glass window of the box (the light path through the refractive index field in the $Z$ direction), and $n_0 = 1.3333$ is the refractive index of pure water at 20 °C.

To illustrate the effect of the above systematic errors on the PIV measurements, we present in Fig. 11a both measured (uncorrected, black-filled symbols) and corrected (open symbols) velocity profiles. The refractive index variation as a function of the vertical coordinate was calculated from the measured temperature and concentration profiles (see Fig. 11b and c) using the empirical formula given by [16]:

$$\begin{aligned} n = n_0 &- 9.184(10)^{-5}(T-20) - 1.833(10)^{-6}(T-20)^2 \\ &+ 1.27(10)^{-8}(T-20)^3 + 0.1748(C/100) \\ &- 2.09(10)^{-3}(C/100)^2 + 6.9(10)^{-2}(C/100)^3 \\ &- 9(10)^{-5}(T-20)(C/100)^{0.5}, \end{aligned}$$

where $T$ is the temperature in degrees Celsius and $C$ is the concentration in weight percents.

Fig. 11 shows that the optical distortion is relatively small and mainly manifested within the region of the concentration gradient layer. Since the unstable regions (where vortices are generated) are outside this layer, the effect of the systematic error on our analyses is negligible.

## References


[1] C.F. Chen, D.G. Briggs, R.A. Wirtz, Stability of thermal convection in a salinity gradient due to lateral heating, Int. J. Heat Mass Transfer 14 (1971) 57–65.

[2] R.A. Wirtz, C.S. Reddy, Experiments on convective layer formation and merging in a differentially heated slot, J. Fluid Mech. 91 (3) (1979) 451–464.

[3] J. Tanny, A. Tsinober, The dynamics and structure of double-diffusive layers in side wall-heating experiments, J. Fluid Mech. 196 (1988) 135–156.

[4] J. Tanny, A. Tsinober, On the behavior of a system of double-diffusive layers during its evolution, Phys. Fluids A 1 (3) (1989) 606–609.

[5] S.G. Schladow, E. Thomas, J.R. Koseff, The dynamics of intrusions into a thermohaline stratification, J. Fluid Mech. 236 (1992) 127–165.

[6] E.J. Kranenborg, H.A. Dijkstra, On the evolution of double-diffusive intrusions into a stably stratified liquid: a study of the layer merging process, Int. J. Heat Mass Transfer 41 (1998) 2743–2756.

[7] C.L. Chan, W.-Y. Chen, C.F. Chen, Secondary motion in convection layers generated by lateral heating of a solute gradient, J. Fluid Mech. 455 (2002) 1–19.

[8] T.L. Bergman, A. Ungan, A note on lateral heating in a double-diffusive system, J. Fluid Mech. 194 (1988) 175–186.

[9] K. Kamakura, H. Ozoe, Double-diffusive natural convection between vertical parallel walls—experimental study of two-layer convection, J. Chem. Eng. Jpn. 24 (5) (1991) 622–627.

[10] T. Nishimura, Y. Ogata, S. Sakura, A.M. Morega, Interfacial breakdown of double-diffusive convective layers by a horizontal temperature gradient, Int. J. Heat Mass Transfer 42 (1999) 1479–1489.

[11] T. Nishimura, S. Sakura, K. Gotoh, A.M. Morega, Traveling plumes generated within a double diffusive interface between counter shear flows, Phys. Fluids 12 (11) (2000) 3078–3081.

[12] T. Nishimura, S. Sakura, Y. Ogata, Mass transfer through the diffusive interface in a two-layer, salt-stratified system under a horizontal temperature gradient, Chem. Eng. Sci. 55 (2000) 5301–5309.

[13] J. Tanny, B. Yakubov, Experimental study of a double-diffusive two-layer system in a laterally heated enclosure, Int. J. Heat Mass Transfer 42 (1999) 3619–3629.

[14] J. Tanny, B. Yakubov, The effect of layer depth on mixing in a double-diffusive two-layer system, Int. J. Heat Mass Transfer 45 (2002) 2101–2105.

[15] M.J. Head, The use of miniature four-electrode conductivity probes for high resolution measurements of turbulent density or temperature variations in salt-stratified water flows, Ph.D. thesis, University of California, San Diego, 1983.

[16] B.R. Ruddick, T.G.L. Shirtcliffe, Data for double diffusers: physical properties of aqueous salt–sugar solutions, Deep-Sea Res. 26 (A) (1979) 775–787.

[17] R.C. Weast, Handbook of Chemistry and Physics, Cleveland, CRC Press, 1977.

[18] J.W. Deardorff, Gravitational instability between horizontal plates with shear, Phys. Fluids 8 (6) (1965) 1027–1030.

[19] K.S. Gage, W.H. Reid, The stability of thermally stratified Poiseuille flow, J. Fluid Mech. 33 (1) (1968) 21–32.

[20] J.M. Luijkx, J.K. Platten, J.C. Legros, On the existence of thermoconvective rolls, transverse to a superimposed mean

poiseuille flow, Int. J. Heat Mass Transfer 24 (7) (1981) 1287–1291.
[21] A.P. Ingersoll, Convective instabilities in plane Couette flow, Phys. Fluids 9 (1966) 682–689.
[22] I.G. Currie, The effect of heating rate on the stability of stationary fluids, J. Fluid Mech. 29 (2) (1967) 337–347.
[23] E. Palm, On the tendency towards hexagonal cells in steady convection, J. Fluid Mech. 8 (1960) 183–192.
[24] G.E. Elsinga, B.W. van Oudheusden, F. Scarano, Evaluation of aero-optical distortion effects in PIV, in: 12th International Symposium on Applications of Laser Techniques to Fluid Mechanics, Lisbon, Portugal, 12–15 July 2004.